The mantle transition zone beneath eastern North America: Receiver functions and tomographic velocity models

Alexander L. Burky, Jessica C. E. Irving, and Frederik J. Simons

This document contains 21 Figures and 1 Table as a supplement to the Main Text. Each of the figures is referenced in the Main Text, and a thorough description of each figure is provided in the captions. The video animations mentioned in the Main Text can be found on the site where this Supplement was accessed.
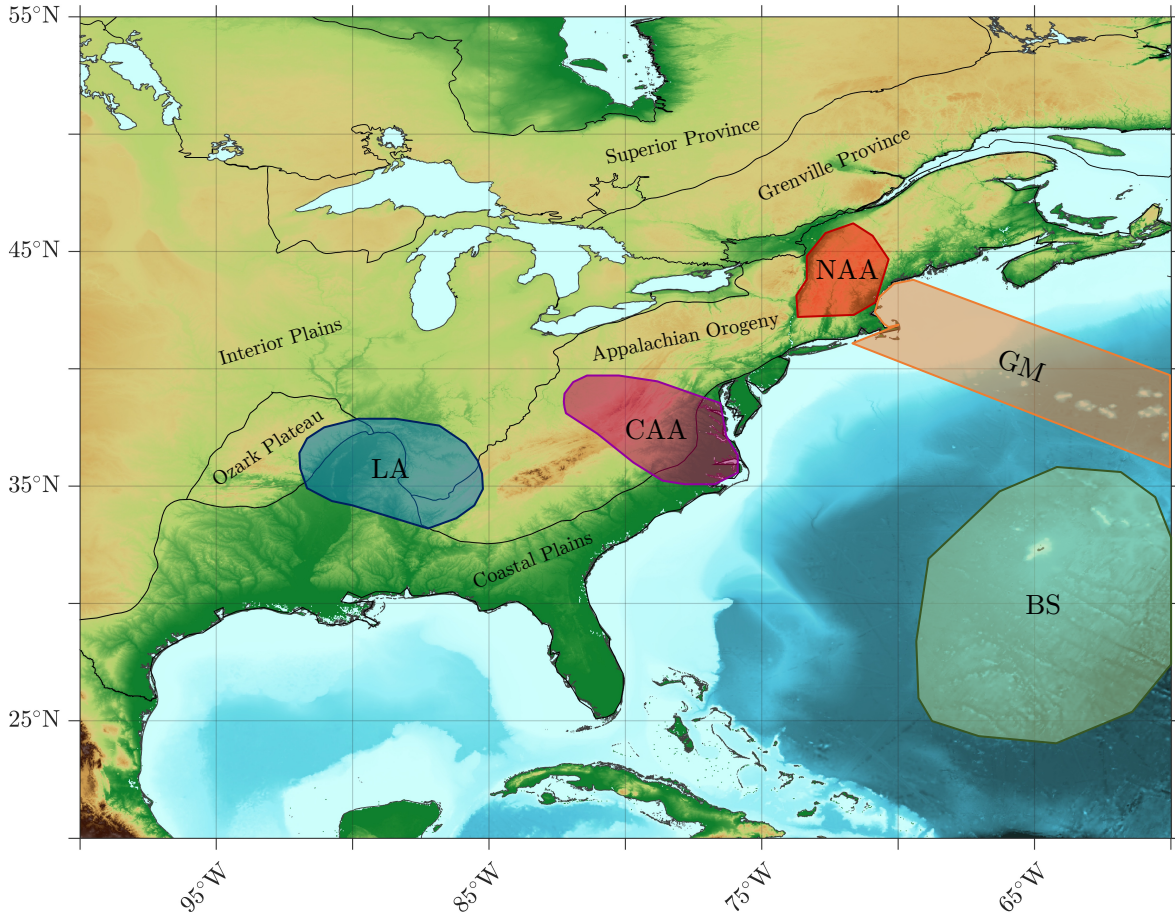

Figure S1: Summary map showing the tectonic provinces of eastern North America and the western Atlantic, overlain with markers indicating the MTZ features mentioned in the Main Text. The labels represent, BS: Bermuda Swell, CAA: Central Appalachian Anomaly, GM: Great Meteor hotspot track, LA: Laramide slab Anomaly, and NAA: Northern Appalachian Anomaly, respectively. The connection between the offshore magmatic events and the Appalachian anomalies remains uncertain, and could be better understood with offshore seismic deployments in the region.

North American Mantle Transition Zone Thickness Observations				
3-D model	GLADM25	GyPSuM	LLNL_G3D_JPS	SL2013NA
$\bar{z} + 2\sigma$	259 km	253 km	256 km	252 km
$\bar{z}$	**246 km**	**241 km**	**242 km**	**241 km**
$\bar{z} - 2\sigma$	233 km	229 km	228 km	230 km
Northern Appalachian Anomaly				
$\bar{z} + 2\sigma$	245 km	244 km	244 km	243 km
$\bar{z}$	**238 km**	**236 km**	**235 km**	**238 km**
$\bar{z} - 2\sigma$	231 km	228 km	227 km	232 km
z_{min}	229 km	224 km	223 km	227 km
Central Appalachian Anomaly				
$\bar{z} + 2\sigma$	244 km	244 km	245 km	243 km
$\bar{z}$	**238 km**	**236 km**	**236 km**	**237 km**
$\bar{z} - 2\sigma$	233 km	228 km	227 km	231 km
z_{min}	228 km	216 km	214 km	228 km
Laramide Slab Anomaly				
z_{max}	263 km	257 km	262 km	257 km
$\bar{z} + 2\sigma$	257 km	251 km	256 km	251 km
$\bar{z}$	**249 km**	**246 km**	**248 km**	**245 km**
$\bar{z} - 2\sigma$	240 km	240 km	240 km	240 km

Table S1: Mantle transition zone (MTZ) thickness observations from our study. The top of the table summarizes the entire dataset, and the three sections underneath summarize measurements of the Northern Appalachian Anomaly (NAA), Central Appalachian Anomaly (CAA), and Laramide Slab Anomaly. For the NAA and CAA, statistics are reported ($\bar{z}$ is the mean MTZ thickness, σ the standard deviation, and z_{min} and z_{max} the minima and maxima) for below the 242 km contour line in the enclosed regions shown in Figs S2 and S3. Areas above the 242 km contour line for the region enclosed shown in Fig. S4 are used for the Laramide Slab Anomaly. Note that the minima and maxima associated with all three anomalies are outside of the 2σ range.
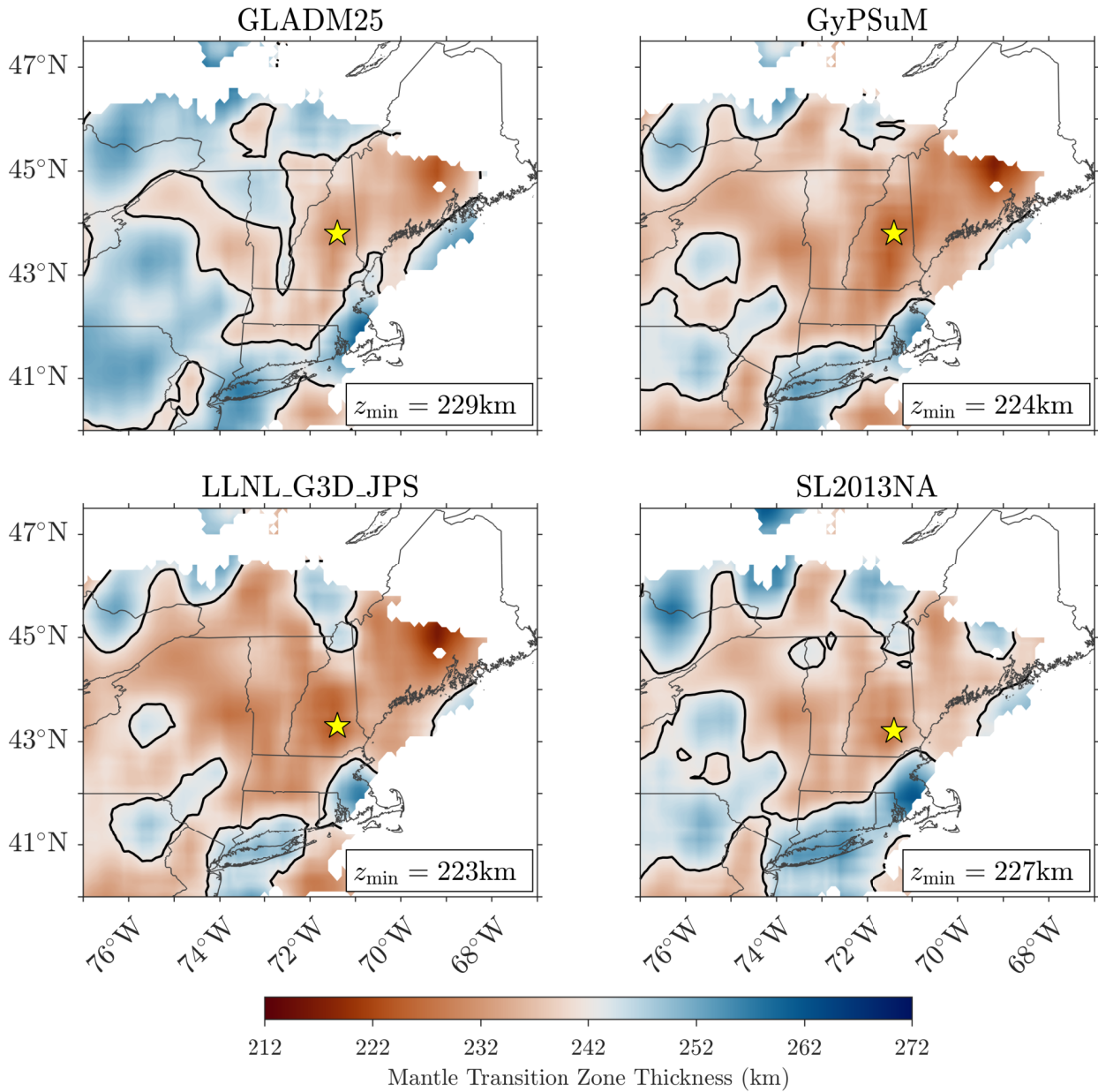
Figure S2: Maps showing the measured MTZ thickness in the region containing the Northern Appalachian Anomaly (NAA), for the four different 3-D models identified in the titles. The stars indicate the locations of the minimum thickness, z_{min}, used in the Main Text to estimate the upper limit on the magnitude of the warm thermal anomaly. We have restricted this measurement to be reasonably far from the edges of this region where data coverage is less robust. The solid black contour lines denote the 242 km level, which corresponds to the global average (Lawrence & Shearer, 2006).
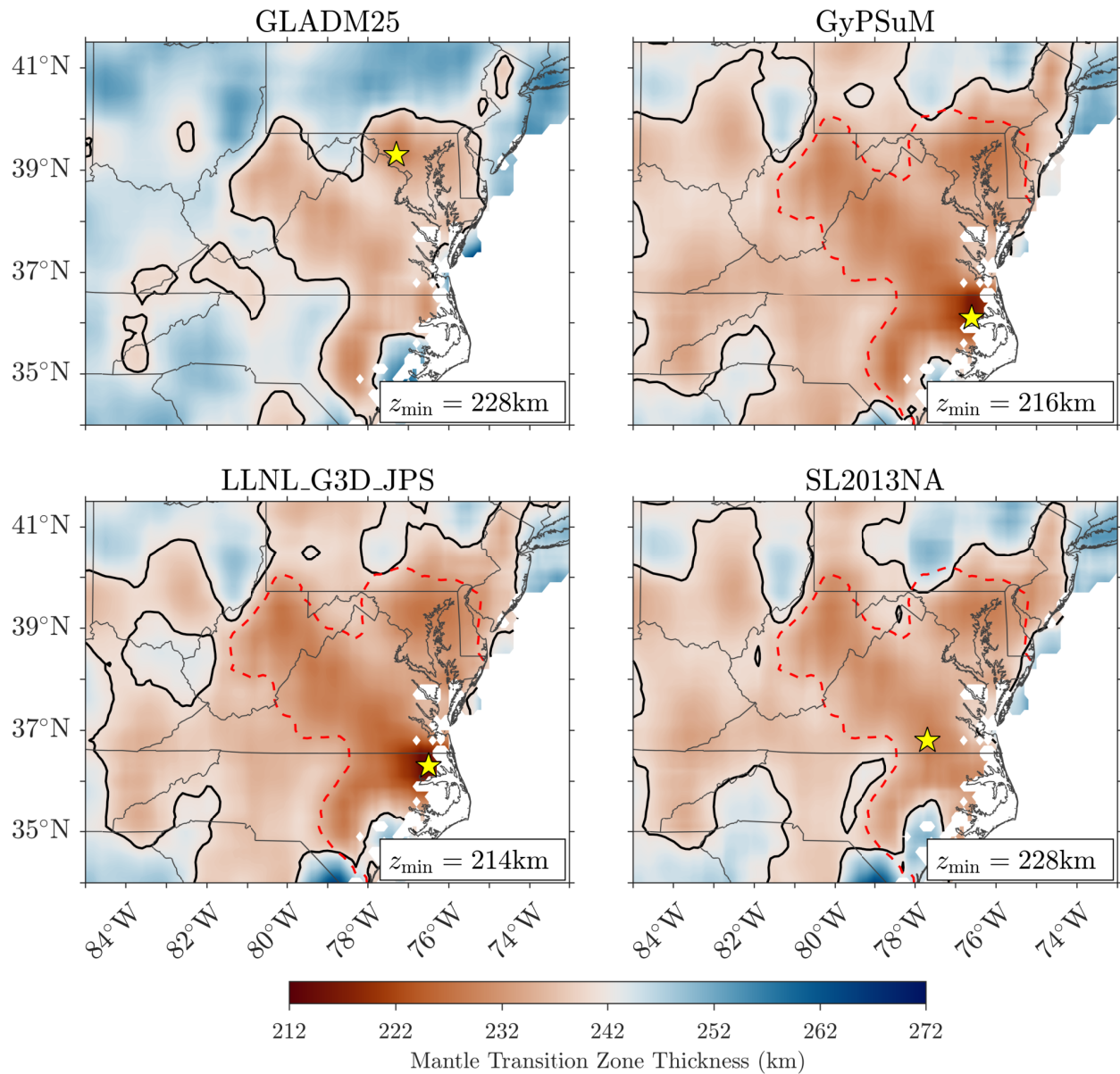
Figure S3: Maps showing the measured MTZ thickness in the region containing the Central Appalachian Anomaly (CAA). Same layout as Fig. S2, however, the black contour line is drawn at 241 km to better highlight the feature in model GLADM25. Note that the thinning is more pronounced when depth-converting with models GyPSuM and LLNL_G3D_JPS, consistent with Fig. S2. The extent of the anomaly is consistent beneath Maryland, Virginia, and eastern West Virginia across all four models. This can be seen from the contour extracted from model GLADM25 (dashed red lines) overlain on the other three models.
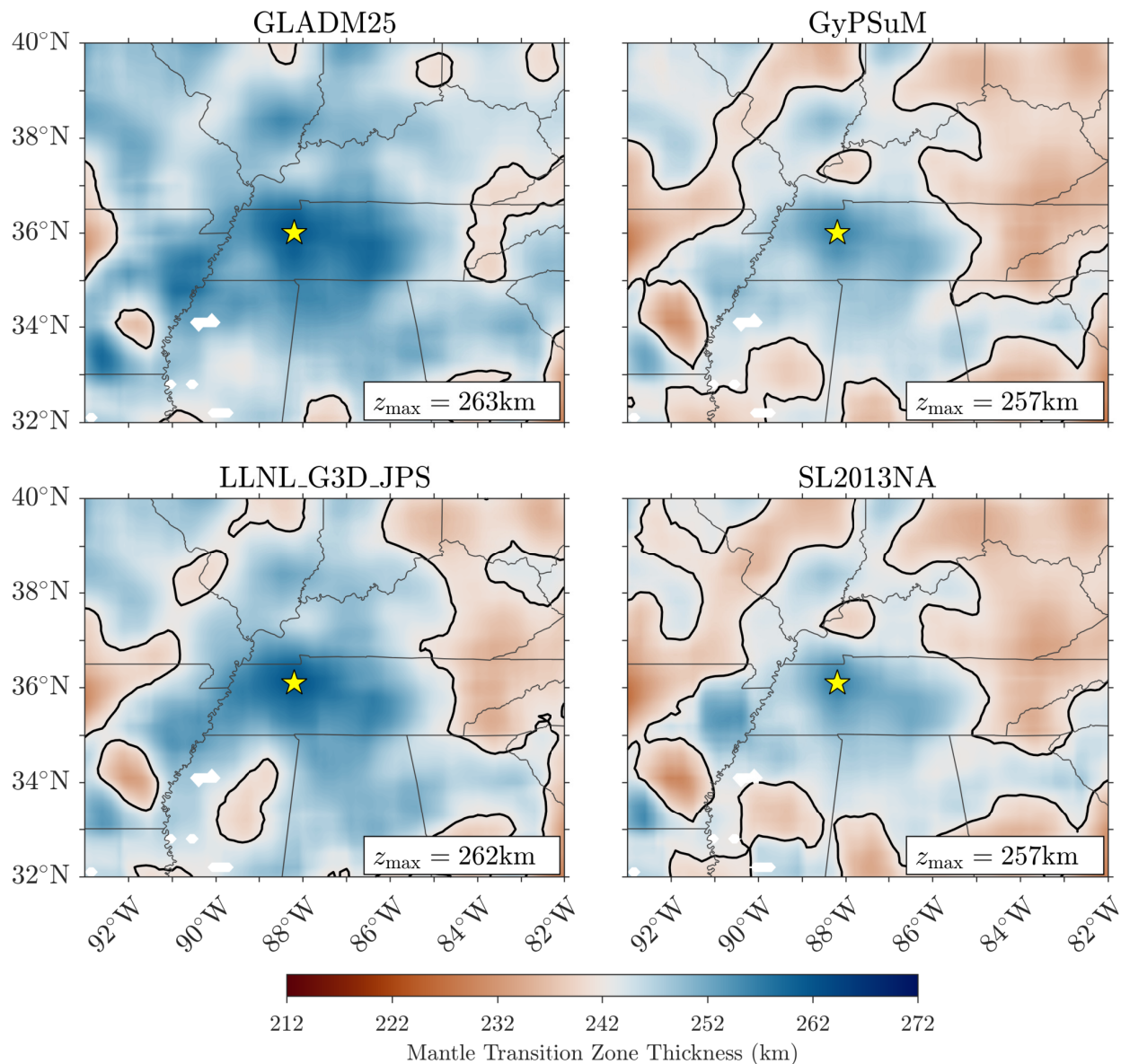
Figure S4: Maps showing the measured MTZ thickness in the region containing the the thickened MTZ anomaly beneath western Tennessee. Same layout as Fig. S2, however, the stars now indicate the locations of the maximum thickness, z_{max}, used in the Main Text to estimate the upper limit on the magnitude of the cold thermal anomaly. Note that the location of the maximum thickness is consistent across all four models, and that the geometry of the anomaly is also roughly consistent. The range of the maximum thickness anomaly (6 km variation) is fairly small between all four models.
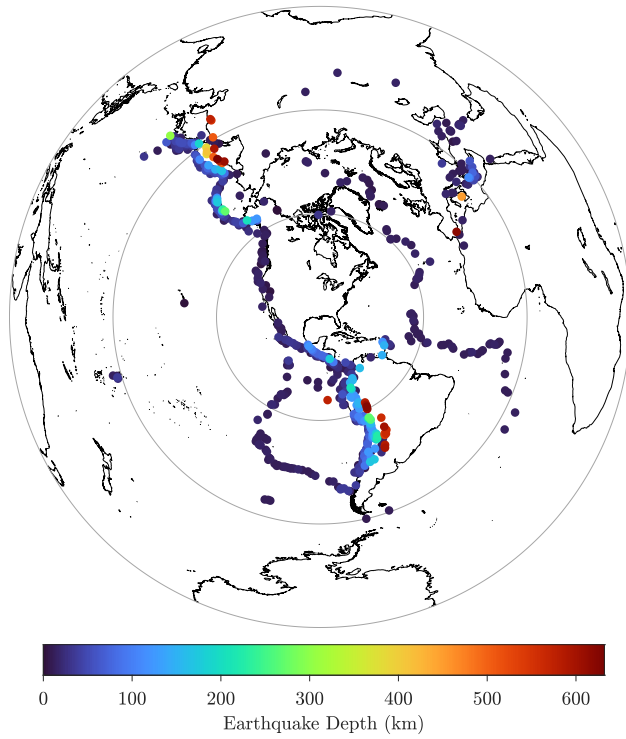
Figure S5: Depths of the earthquakes which contributed to the accepted receiver functions used in our study. Note the increasing depths of earthquakes in subduction zones, as expected, and the shallow depths of earthquakes at mid-ocean ridges.
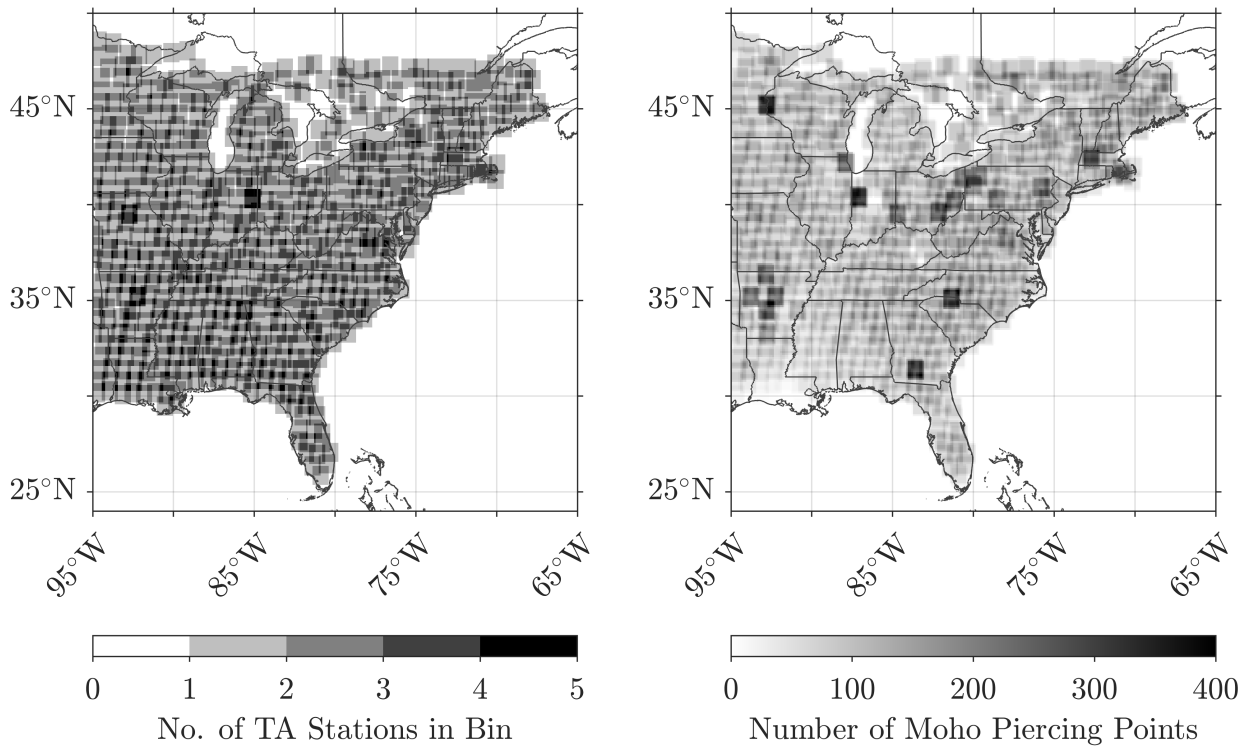

Figure S6: Density maps showing the number of TA stations in each CCP bin (*left*) next to the number of Moho piercing points in each bin (*right*). Certain bins with many stations, combined with exceptional data quality at some stations, lead to the handful of bins with anomalously high numbers of piercing points seen in the figure on the right.

AxiSEM Synthetics: IASP91
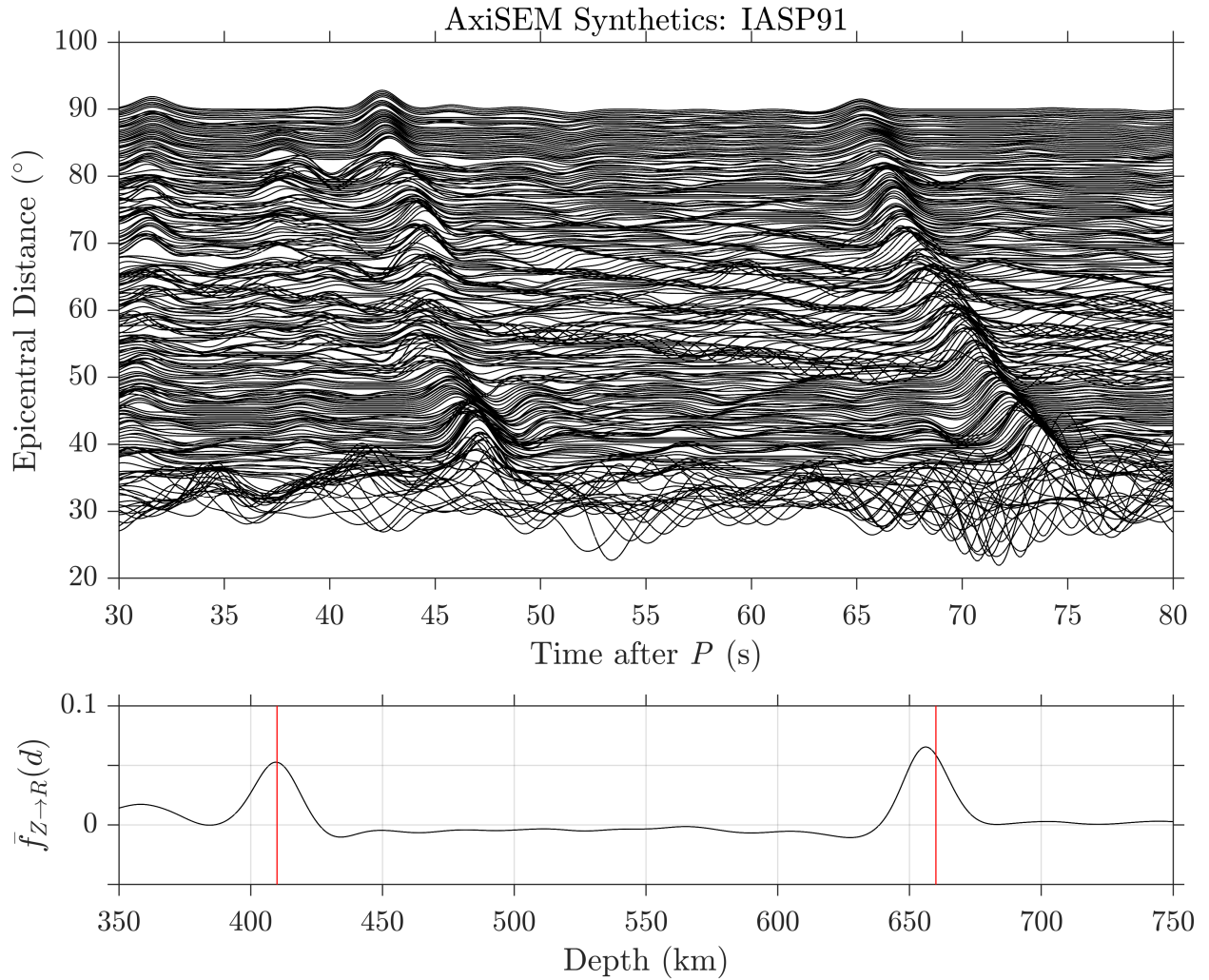
Figure S7: Validation of our methodology for synthetic receiver functions computed from AxiSEM synthetic seismograms (Nissen-Meyer et al., 2014). Synthetics are calculated for model *iasp91* using a 1 Hz dominant period, and are processed using the methodology outlined in the Main Text. Our method is able to successfully resolve the *P410s* and *P660s* phases, with a slight underestimation of the depth of the 660.
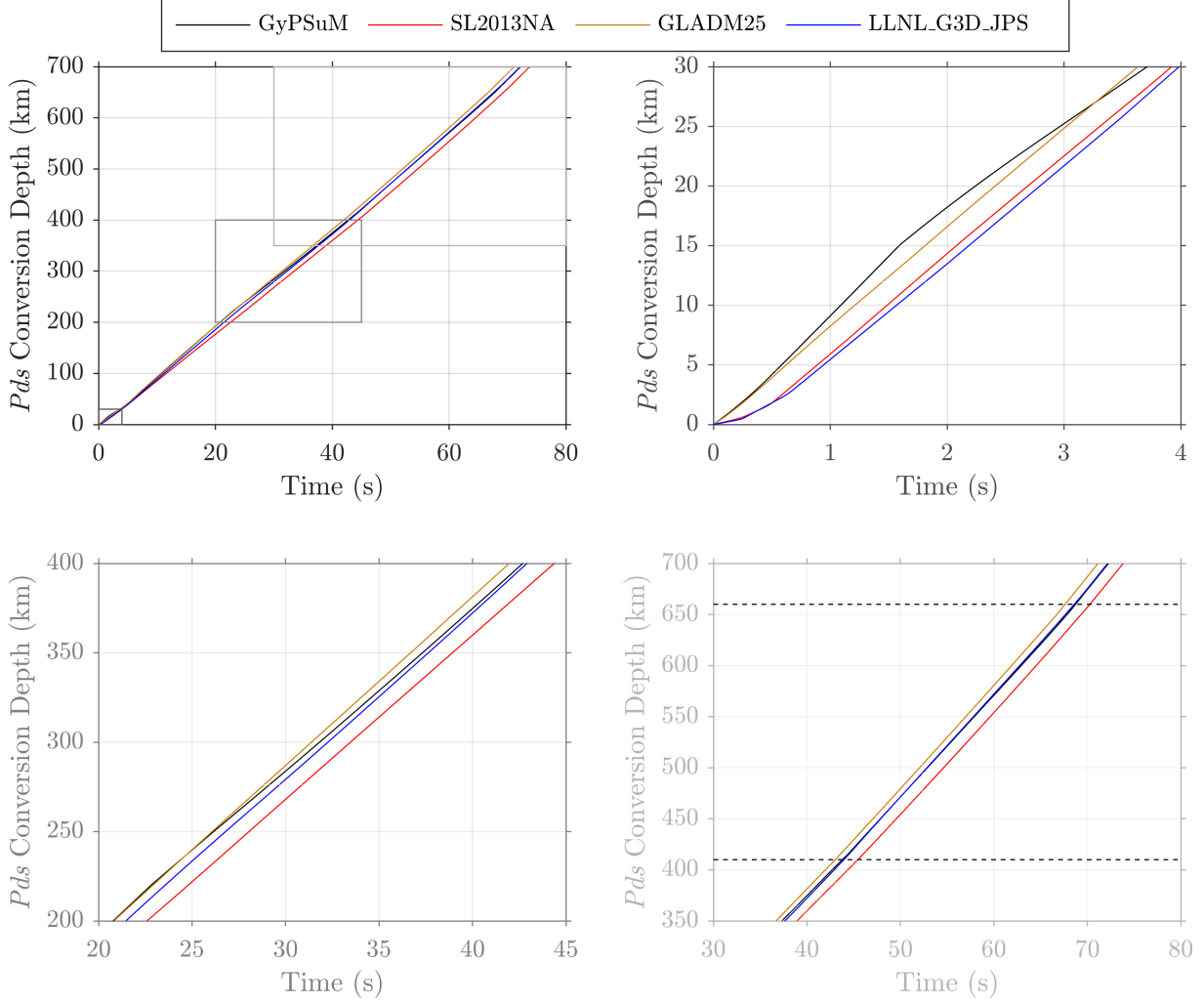
Figure S8: The average relationship between *Pds* conversion depth and time relative to the main *P* arrival for all receiver functions recorded by station TA W41A. These relationships are shown for the four different 3-D velocity models used in our study. They are used to transform receiver functions from the time-domain to the depth-domain. To illustrate how to comprehend these plots, the reader's attention is drawn to the top-right panel. A peak 1 s after the main *P* arrival would be mapped to a depth of ∼5 km using models LLNL_G3D_JPS and SL2013NA, but would be mapped to a depth of ∼9 km with models GLADM25 and GyPSuM. The behavior of these curves in the lower-right panel explains the spread in the 410 and 660 depths seen in Fig. 7 of the Main Text. Since these curves are essentially parallel through the MTZ, the measured MTZ thickness is consistent regardless of the chosen model.
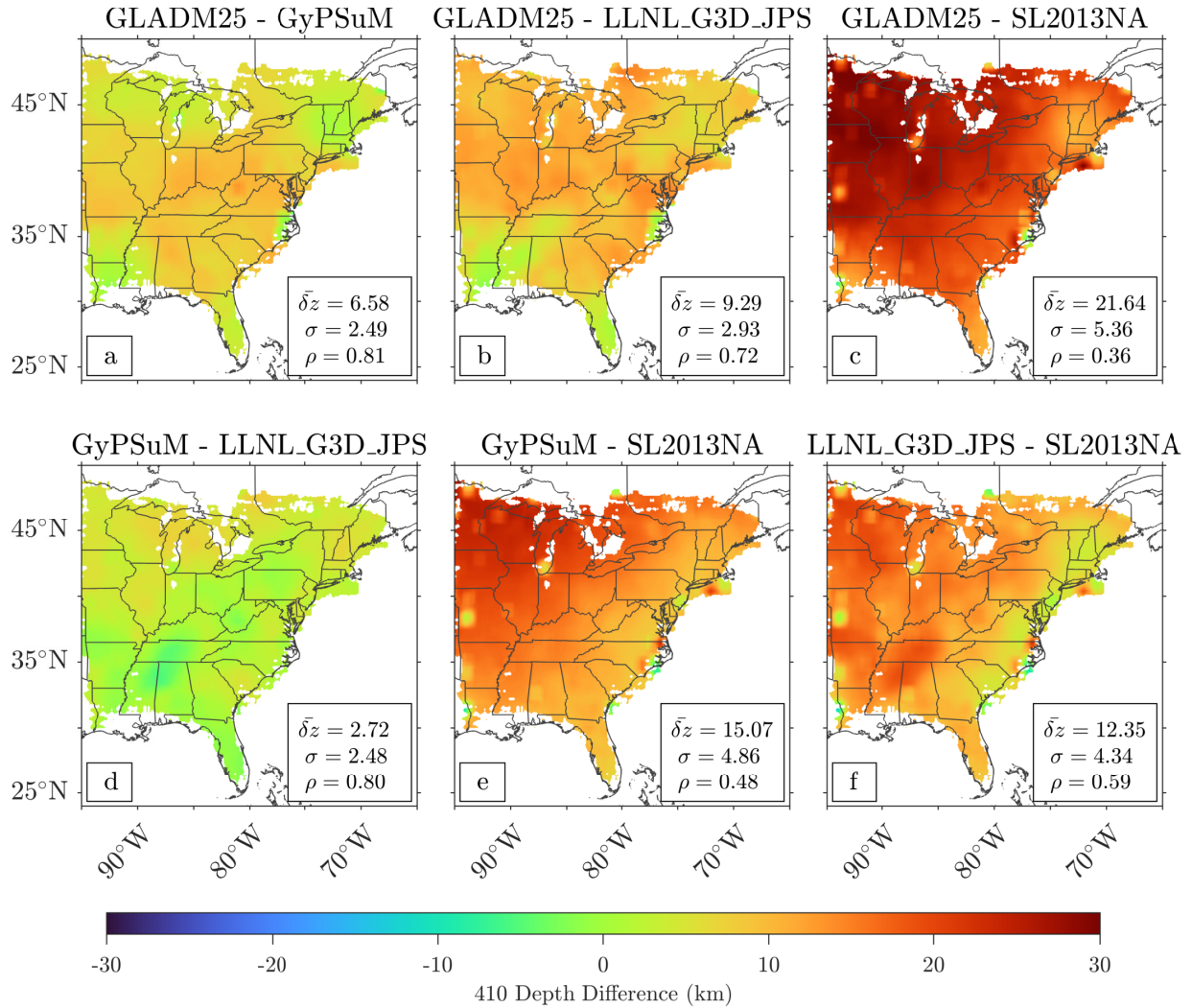
Figure S9: Maps showing the differences in the 410 between each pair of 3-D models, laid out as Fig. 8 of the Main Text. Note that the average differences ($\overline{\delta z}$) between models are greater than they were for the MTZ thickness. The correlation coefficients (ρ) are consistently smaller than for the MTZ thickness, reinforcing the idea that the MTZ thickness is a more robust measurement than the absolute depth of the 410.
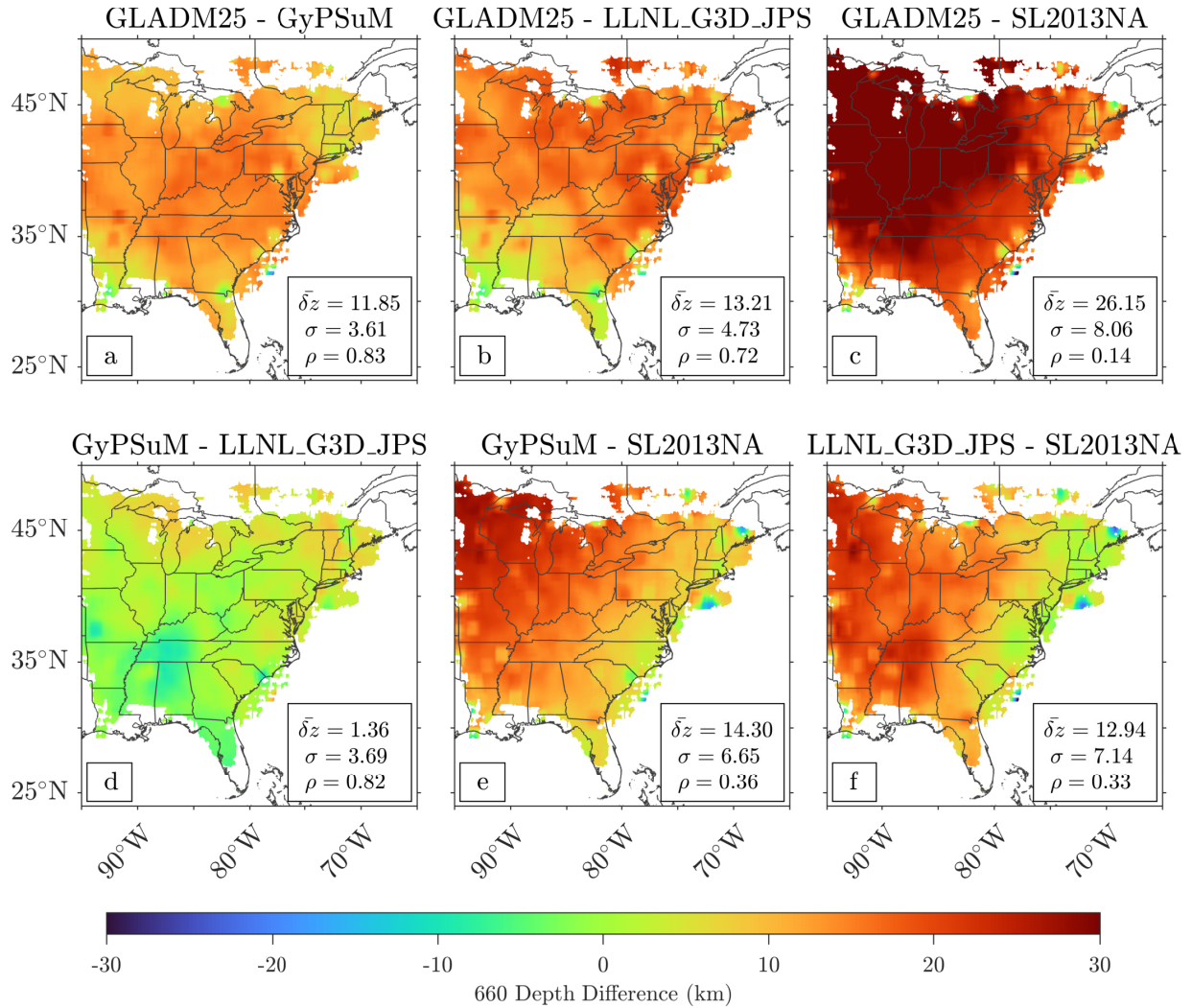
Figure S10: Maps showing the differences in the 660 between each pair of 3-D models, laid out as Fig. S9. Once again note the smaller correlation coefficient between models compared to that of the MTZ thickness shown in Fig. 8 of the Main Text, showing that the MTZ thickness is more robust than the absolute depth of the 660. Model SL2013NA, in particular, shows very poor correlation with the other three models.
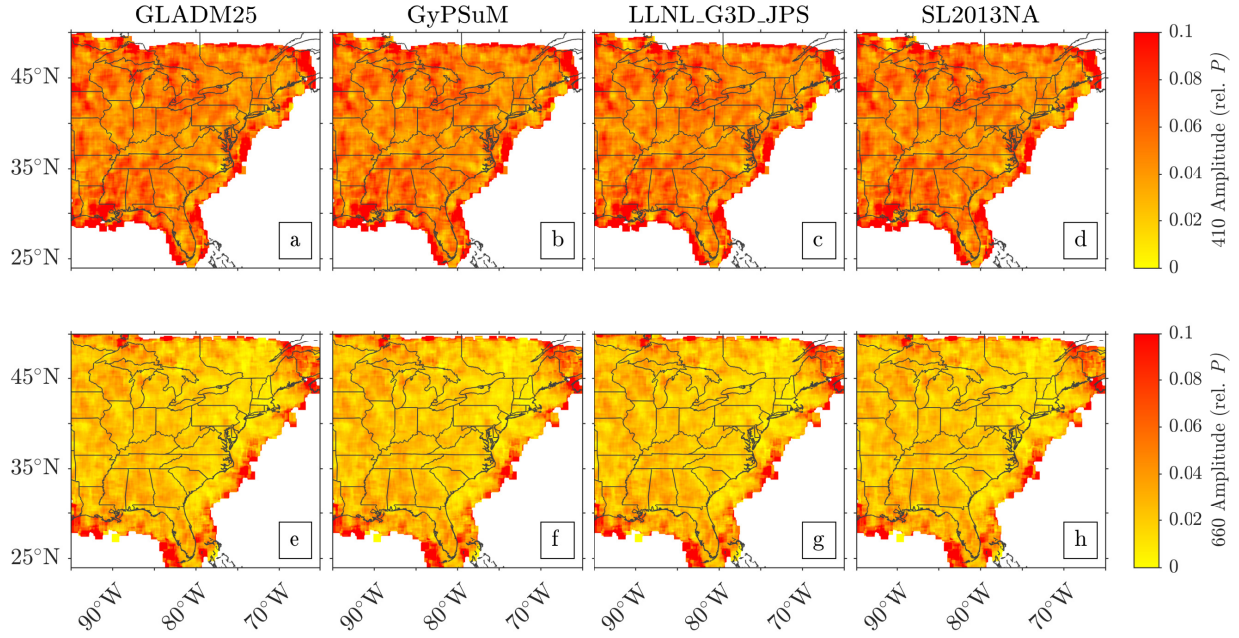
Figure S11: Maps showing the average measured amplitude of the 410 and 660 signals relative to the main P arrival (defined as 1). Note that the 410 signal is consistently larger than the signal from the 660. This can also be seen in the cross sections shown in Figs 4–6 of the Main Text.
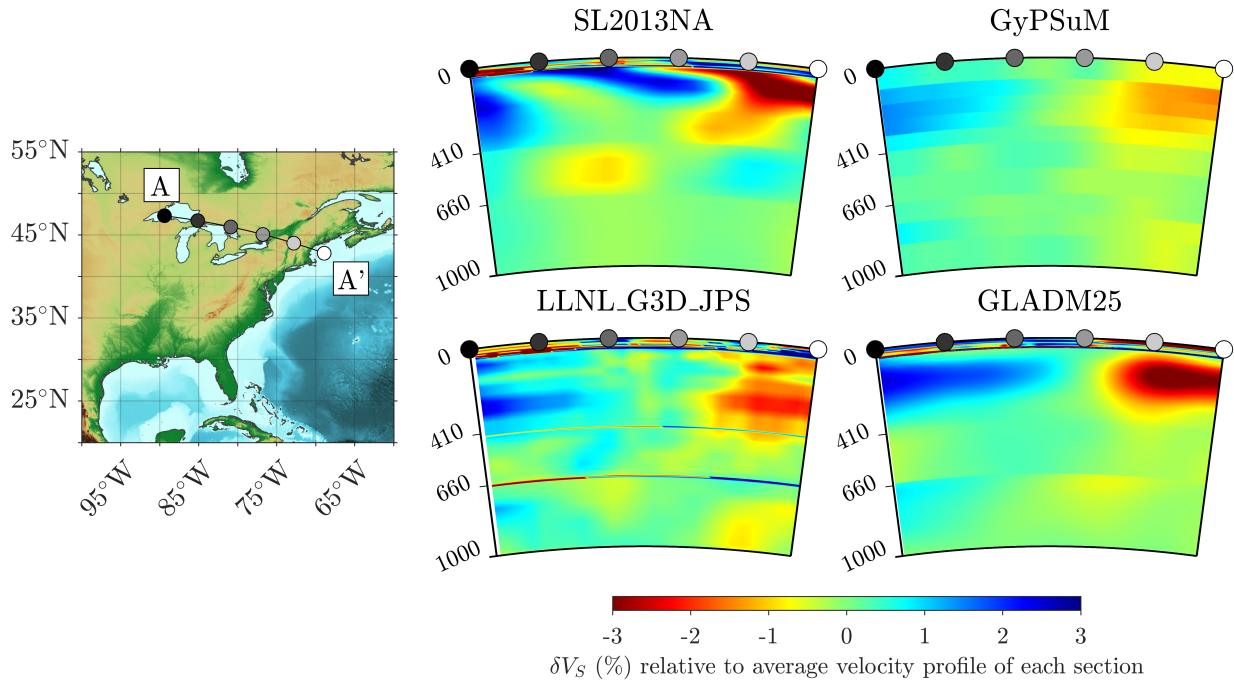

Figure S12: Cross sections along line A-A through the four selected tomography models identified by the titles. Note the presence of a strong low-velocity anomaly beneath New England (the Northern Appalachian Anomaly, NAA). The NAA appears to be confined to the upper mantle above the MTZ, but the receiver function data suggest that it has an effect on the MTZ. Plotted is the percent variation of the S wave velocity from the average one-dimensional velocity profile over the entire cross section.
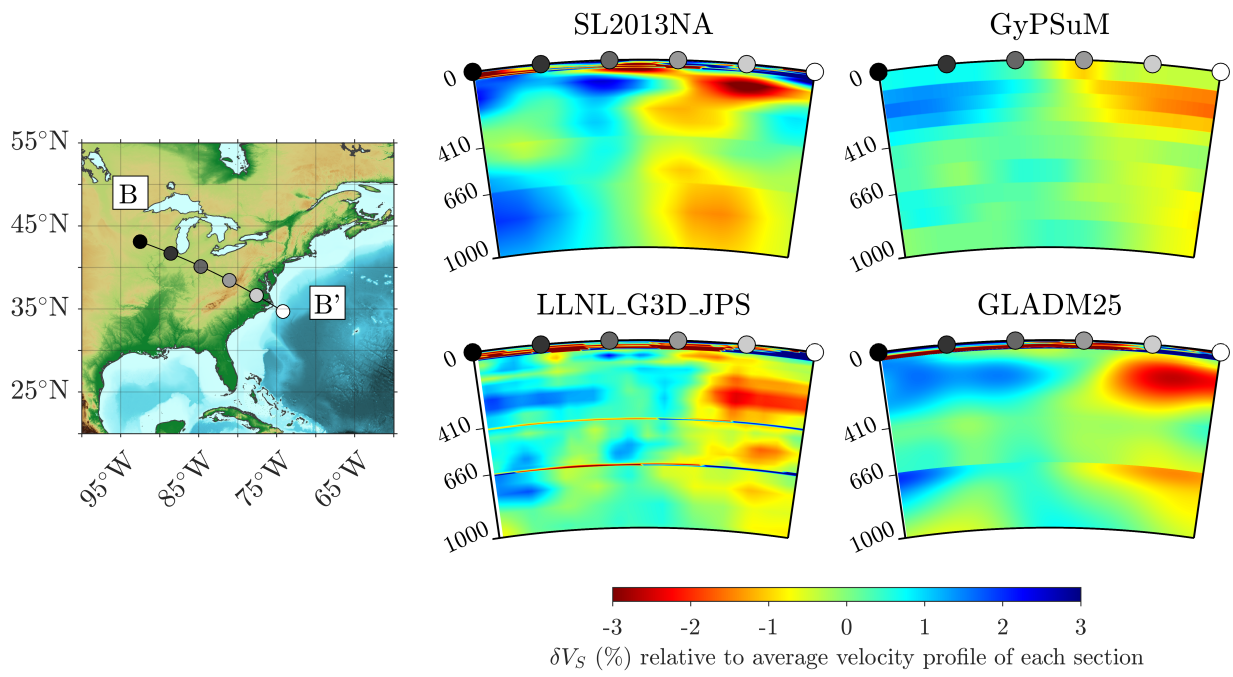
SL2013NA GyPSuM

LLNL_G3D_JPS GLADM25

δV_S (%) relative to average velocity profile of each section

Figure S13: Same as Fig. S12 but for cross section B-B'.

SL2013NA GyPSuM

LLNL_G3D_JPS GLADM25

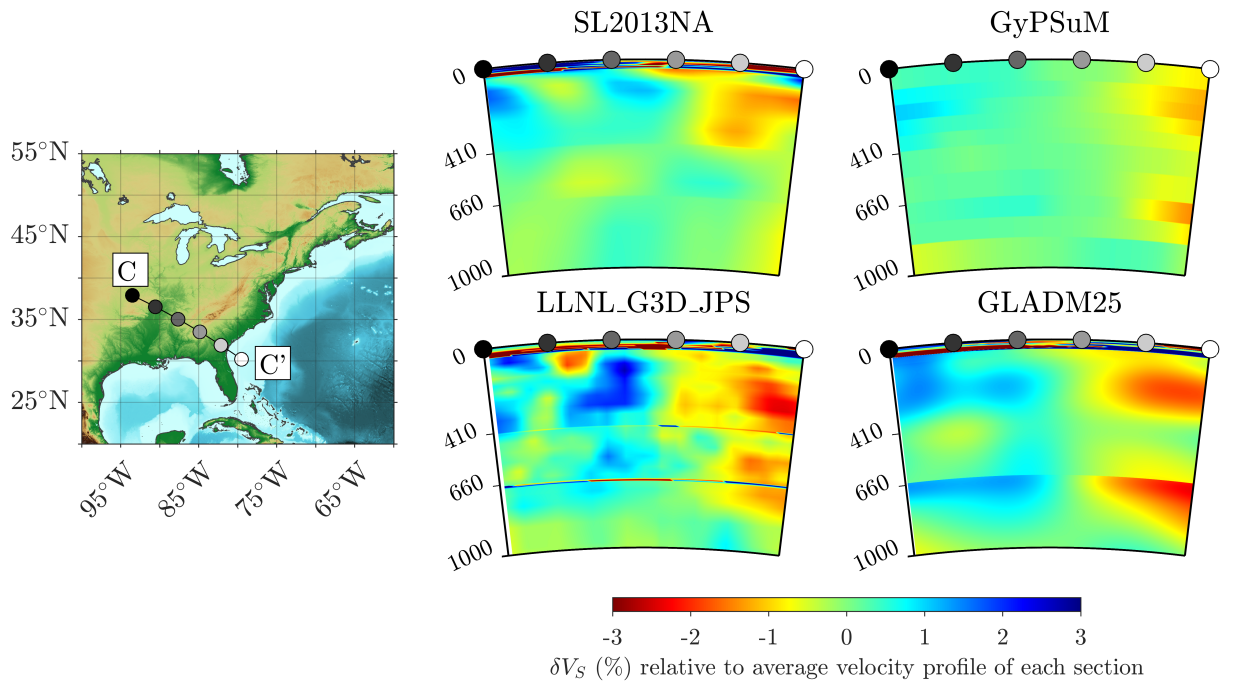δV_S (%) relative to average velocity profile of each section
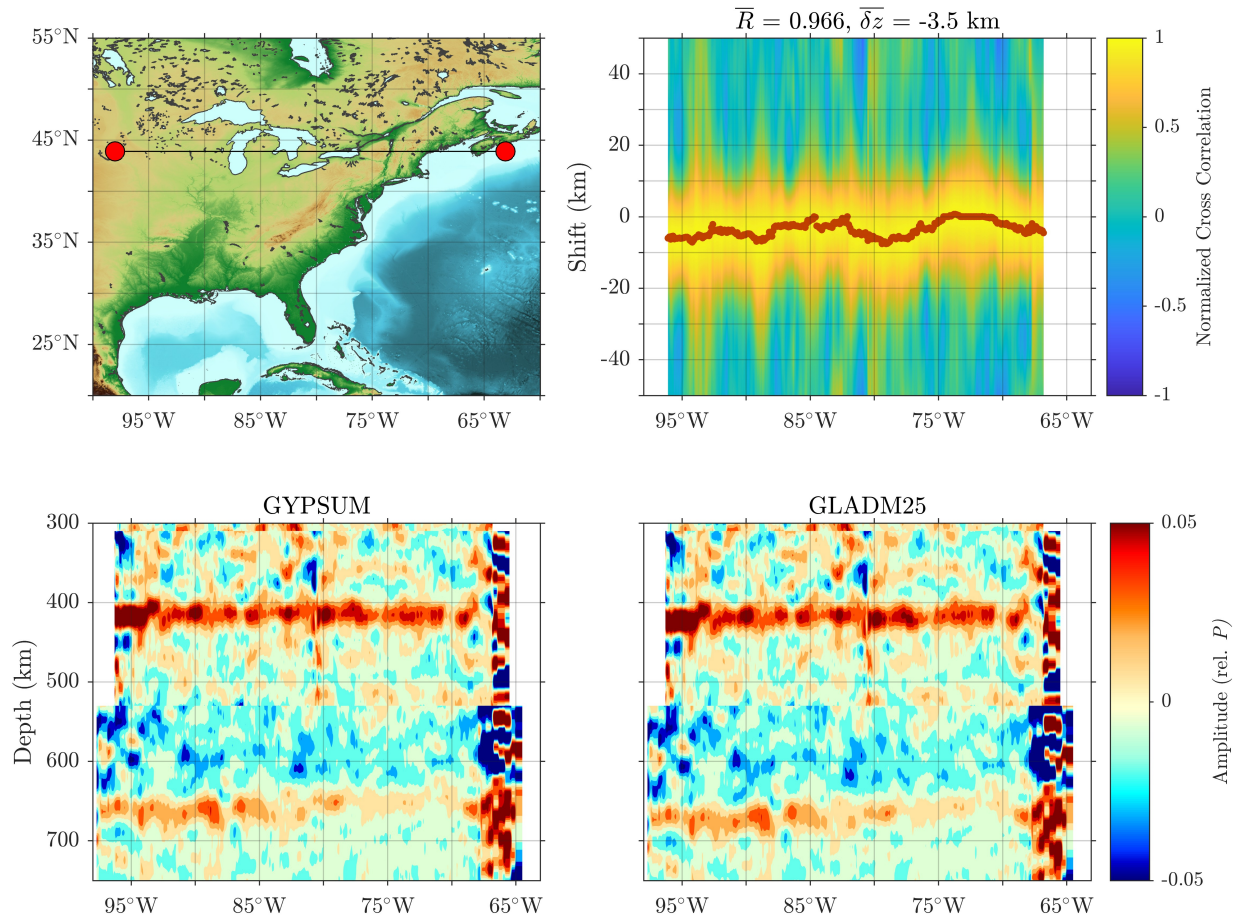
Figure S14: Same as Fig. S12 but for cross section C-C'.

Figure S15: Snapshot from the supplemental videos showing the cross correlation between two CCP stacks. The bottom panel shows the CCP stacks, and the top right panel shows the cross correlation of the two stacks. The red line indicates the maximum of the cross correlation at each longitude. $\bar{R}$ is the average value of the correlation coefficient, and $\bar{\delta z}$ is the average value of the shifts indicated by the red dots. For all of the different CCP stacks, the correlation coefficient tends to be high, but there is a great deal of variability in the relative shifts of the stacks $\bar{\delta z}$.
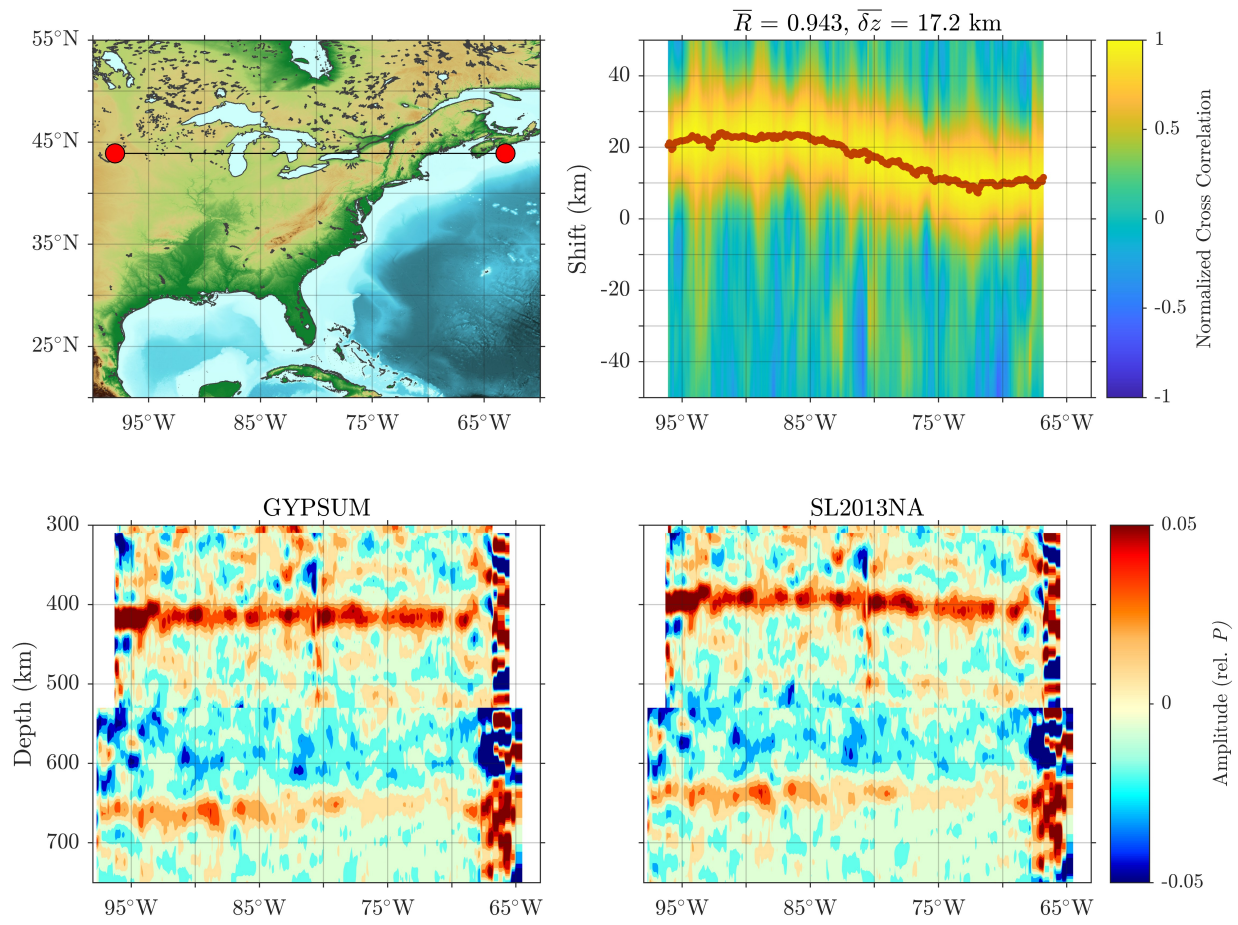
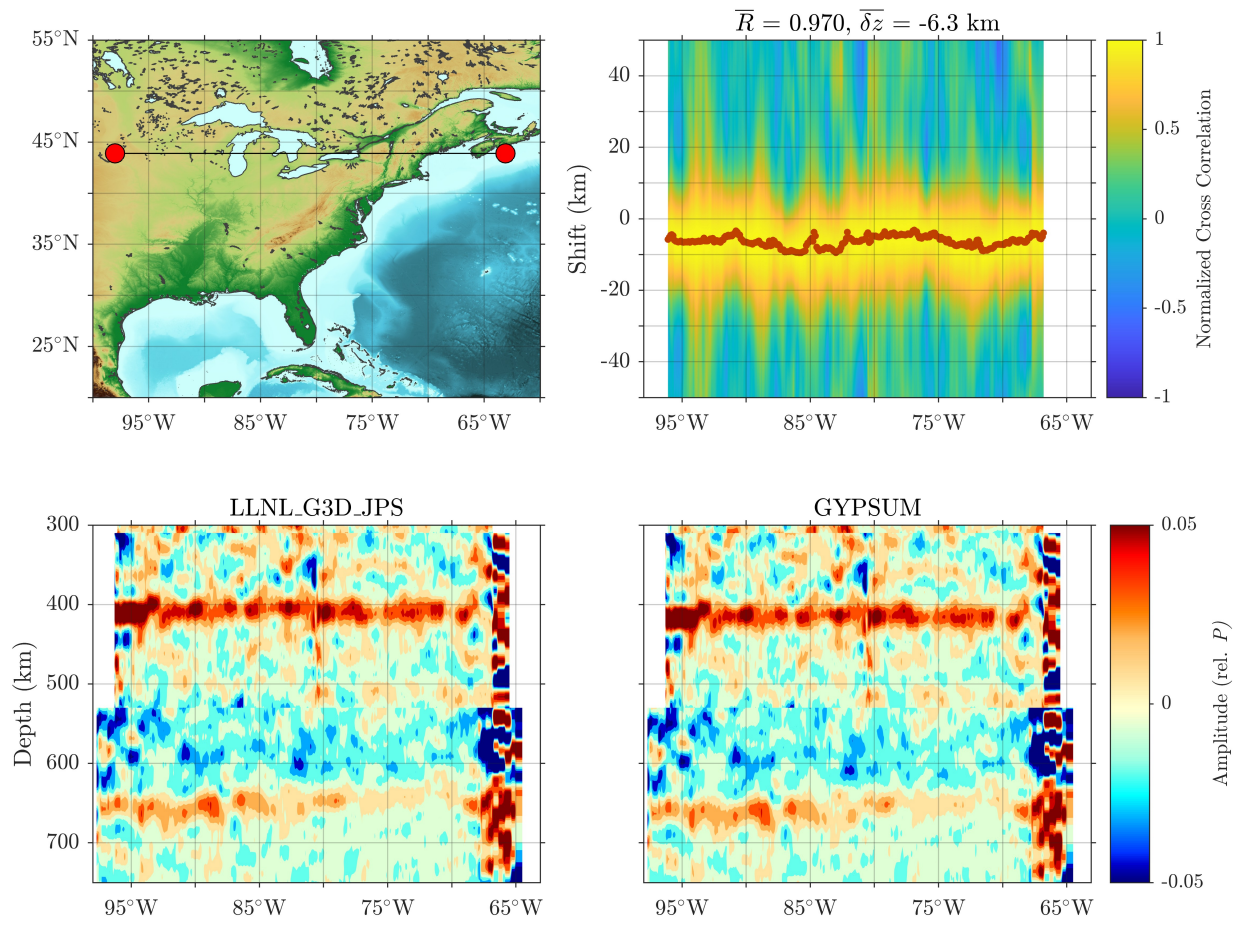Figure S16: Same as Fig. S15 but for models GyPSuM and SL2013NA.

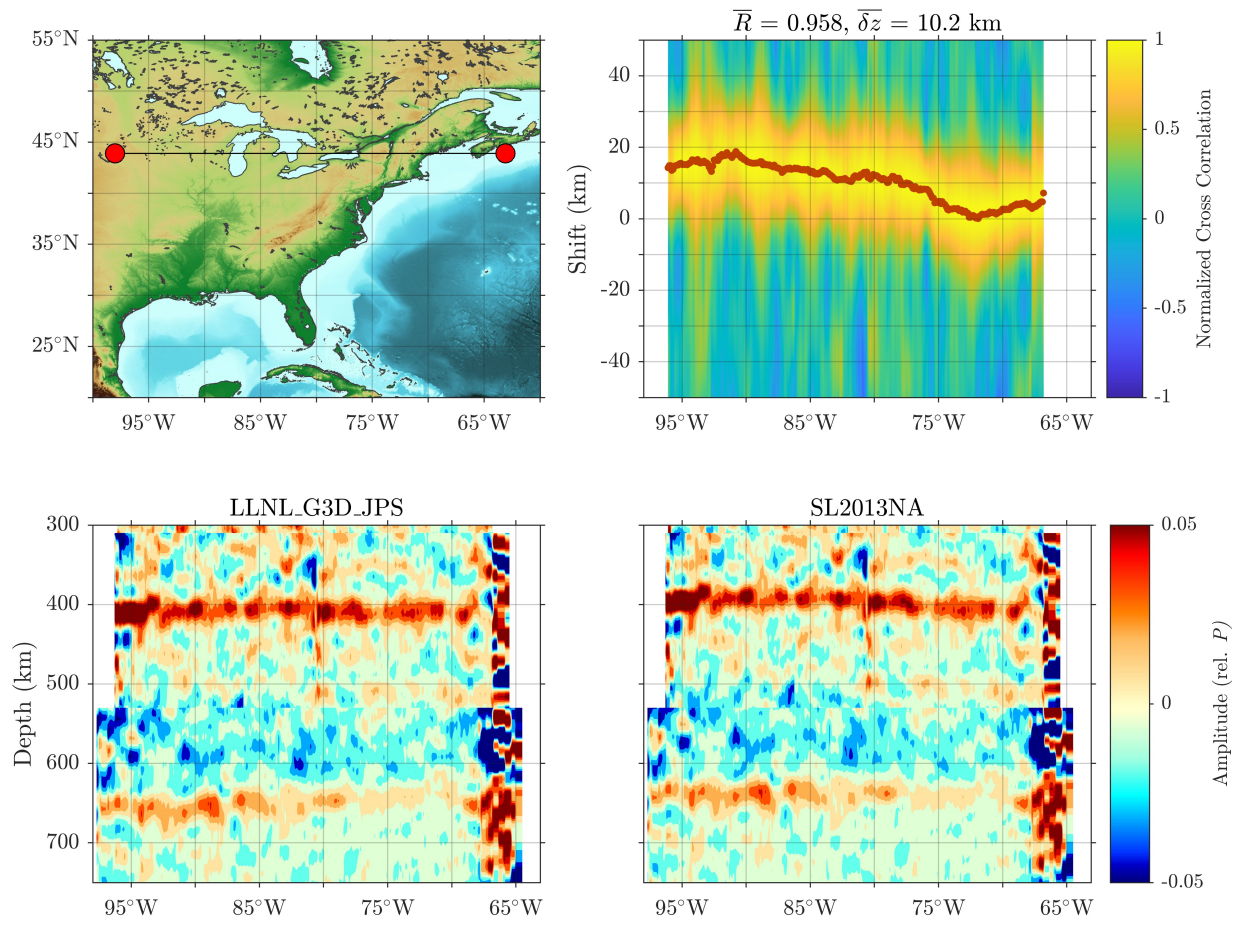Figure S17: Same as Fig. S15 but for models LLNL_G3D_JPS and GyPSuM.

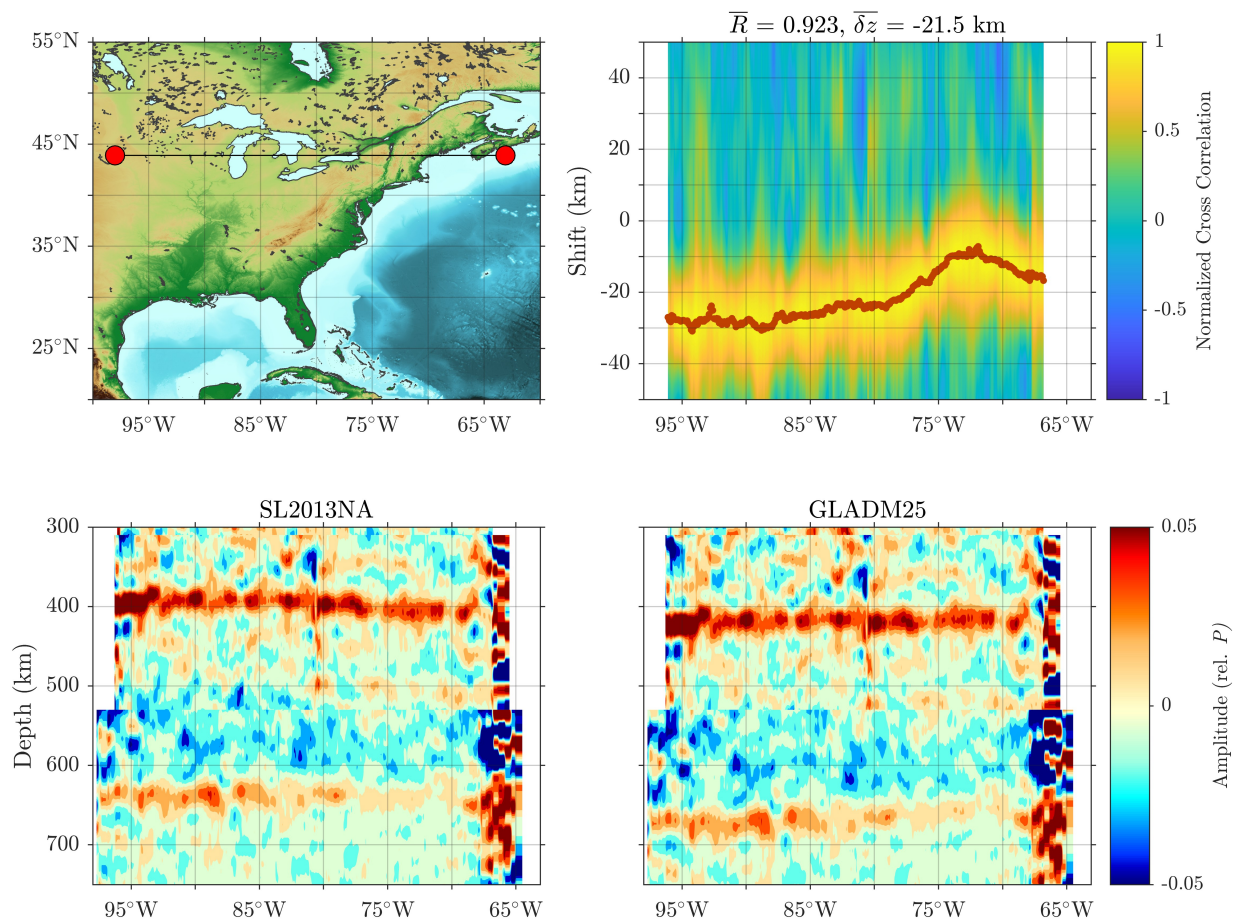Figure S18: Same as Fig. S15 but for models LLNL_G3D_JPS and SL2013NA.

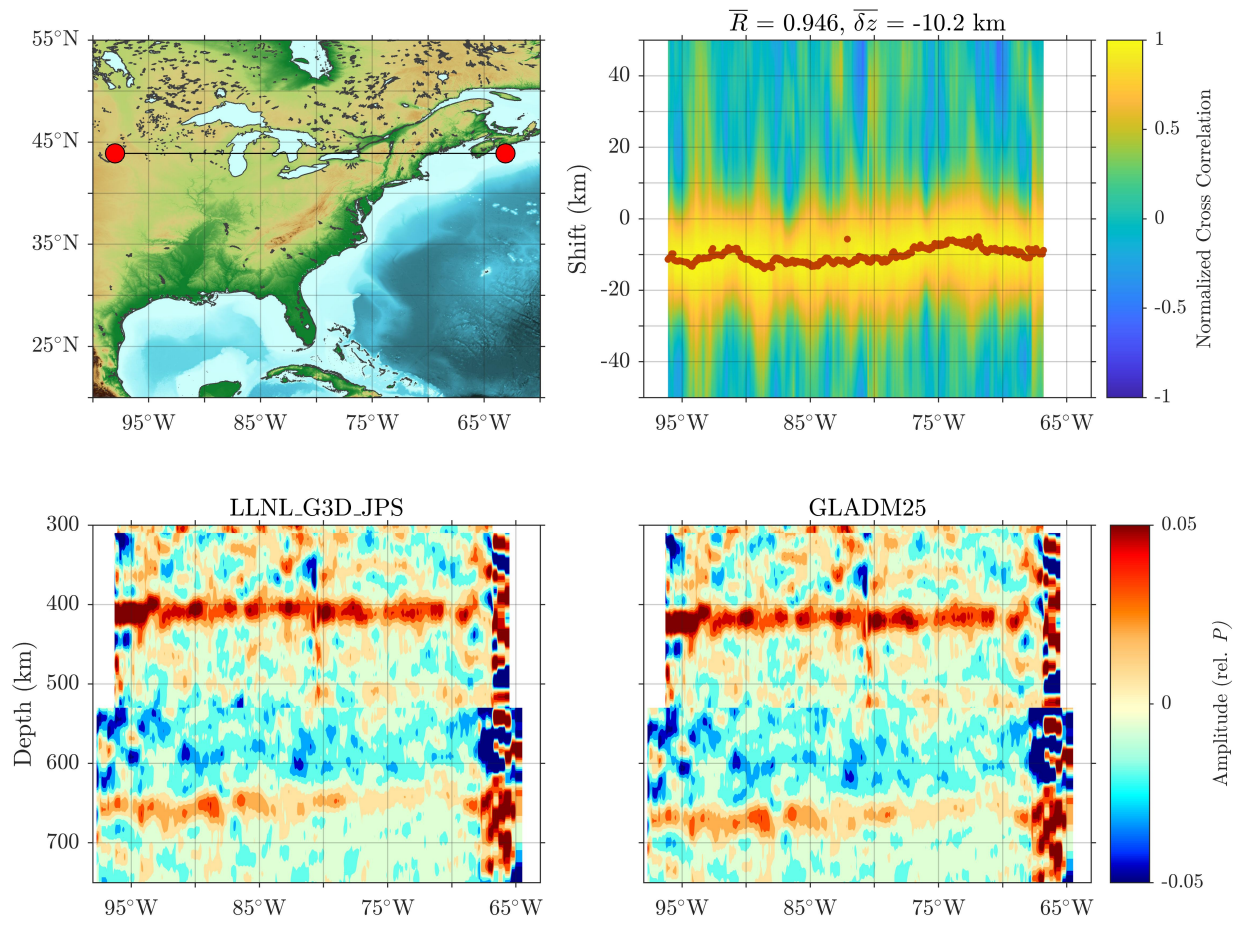Figure S19: Same as Fig. S15 but for models SL2013NA and GLADM25.

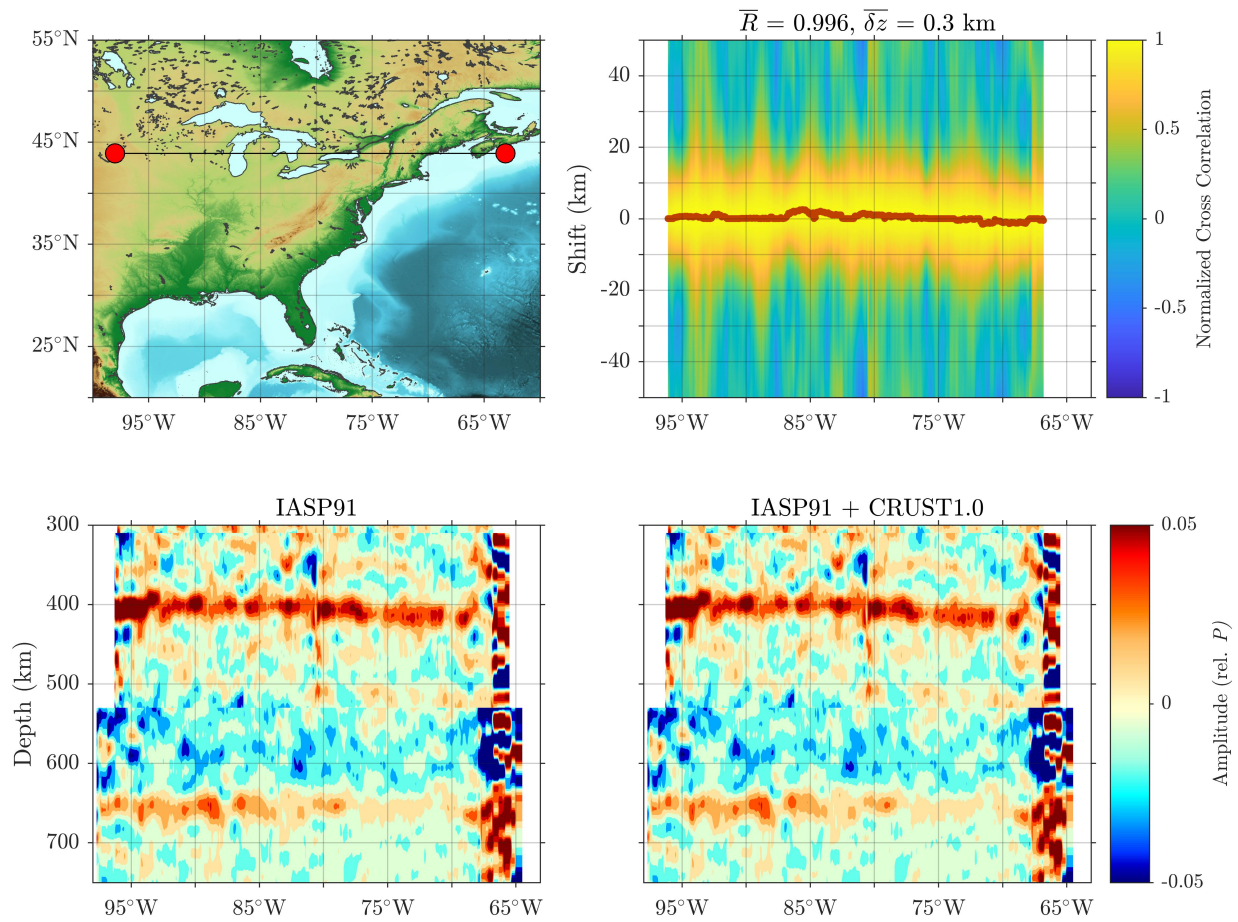Figure S20: Same as Fig. S15 but for models LLNL_G3D_JPS and GLADM25.

Figure S21: Same as Fig. S15 but for models IASP91 and IASP91 + CRUST1.0.

References

Lawrence, J. F., & Shearer, P. M. (2006). A global study of transition zone thickness using receiver functions. *J. Geophys. Res.*, *111*(B06), B06307, doi: 10.1029/2005JB003973.

Nissen-Meyer, T., van Driel, M., Stähler, S. C., Hosseini, K., Hempel, S., Auer, L., ... Fournier, A. (2014). AxiSEM: broadband 3-D seismic wavefields in axisymmetric media. *Solid Earth*, *5*, 425–445, doi: 10.5194/se-5-425-2014.